*Journal of Applied Fluid Mechanics*, Vol. 11, No. 1, pp. 165-176, 2018.
Available online at www.jafmonline.net, ISSN 1735-3572, EISSN 1735-3645.
DOI: 10.29252/jafm.11.01.28079

# Detached Eddy Investigation of Conical Cavity Flow at Mach 0.9

J. Teng[1†], J. Zhang[2], Z. An[2] and Y. You[1]

[1] *School of Aerospace Engineering, Xiamen University, Xiamen, Fujian Province, 361005, P. R. China*
[2] *AECC Hunan Aviation Powerplant Research Institute, Zhuzhou, Hunan Province, 412000, P. R. China*

†*Corresponding Author Email: tengjian@ymail.com*

(Received June 4, 2017; accepted September 3, 2017)

## ABSTRACT

An improved delayed detached eddy simulation (IDDES) is carried out to investigate both the mean and the instantaneous flow characteristics of conical cavities fixed on a cone surface in a Mach 0.9 freestream. Two model categories, a single cavity model with different length (L) to depth (D) ratio and a multi-cavity model that inserted the separation disk into a single cavity are studied. Results indicate that in case of a single cavity model, the cavity L/D ratio is the key parameter that influences mean flow structure and oscillatory characteristics. The bulk reverse flow structure can be broken up into smaller structures as L/D value reduces from 4.0 to 0.51 inside the cavity. Smaller longitudinal pressure gradients on the cavity wall and the thicker downstream boundary layer are observed when larger L/D values are present. The cavities with smaller L/D values can stimulate the pressure oscillation fundamental frequency as well as the acoustic tones to increase the value. Multi-cavity configurations through insertion of a separation disk into the single cavity are helpful in cutting the large reverse flow structure inside a cavity into a smaller, similar, coherent structure, and to reduce the overall cone drag. The insertion of the separation disk can modulate pressure oscillation peaks and sound pressure levels to higher frequency, however, they are not able to reduce the overall sound pressure inside the cavity. Pressure oscillations within each cavity of the multi-cavity configuration have a weak correlation.

**Keywords**: IDDES; Cavity flow; Conical Cavity; Pressure oscillation; Aeroacoustics.

## NOMENCLATURE

| | |
|---|---|
| *CFD* | Computational Fluid Dynamics |
| *D* | cavity depth |
| *DES* | Detached Eddy Simulation |
| *IDDES* | Improved Delayed Detached Eddy Simulation |
| *L* | cavity length |
| *LES* | Large Eddy Simulation |
| *MRD* | Multiple-Row Disk |
| *OASPL* | Overall Sound Pressure Level |
| *PSD* | Power Spectral Density |
| *RANS* | Reynolds-Averaged Navier-Stokes |
| *SPL* | Sound Pressure Level |
| *URANS* | Unsteady Reynolds-Averaged Navier-Stokes |
| *WMLES* | Wall modeled Large Eddy Simulation |

## 1. INTRODUCTION

A cavity is a type of widely applied structure that can be found in the aerospace industry in applications such as weapon bays, landing gear wells, section juncture gaps, pressure vents, and internally installed cavity flame holders in high-speed propulsion systems (Lawson, 2011). Generally, cavities can be divided into three major categories according to cavity length (L) to depth (D) ratio, specifically, open cavity (L/D<10), transitional cavity (10<L/D<13),) and closed cavity (L/D>13) (Stallings, 1987). The precise L/D value for this division varies slightly in different flow speed regimes (Sarohia, 1977), however, the division concept remains the same. In the open cavity, the boundary layer separates from the upstream corner and reattaches near the downstream corner. In the close cavity, the separated boundary first touches the cavity bottom wall and then separates again before the aft wall (Sarohia, 1977). The open cavity can be roughly

divided into two sub-categories, the shallow cavity (L/D>1) and the deep cavity (L/D<1) (Sarohia, 1977). The primary flow feature associated with each cavity is the unsteadiness behavior where the evident flow oscillation and noise can be generated (Heller, 1975). Rockwell (1978) summarized the unstable flow characteristics over and near the cavity structure and categorized the associate self-sustaining oscillation phenomena into fluid-dynamic, fluid-resonant, and fluid-elastic groups. In fluid-dynamic oscillation, the unsteadiness of the cavity shear layer separating at the leading edge is further amplified through K-H instability (Le, 2005). The separated shear layer hits the cavity aft corner and emits strong acoustic waves for the feedback mechanism. Fluid-resonant occurs where the acoustic wavelength is the same order or smaller than the characteristic cavity length (Rockwell, 1978). The fluid-elastic oscillations are principally related to the fluid and elastic boundary interaction (Rockwell, 1978). Insight into the cavity flow unsteadiness nature (Maull, 1963, Heller, 1975, Rockwell, 1977), oscillation frequency (Rossiter, 1962, Heller, 1970), and acoustic feature (Sarohia, 1977, Unalmis, 2001, Larsson, 2004) fostered the development for drag reduction (Charib, 1987), oscillation alleviation (Lamp, 1997, Sarno, 1994), and noise control (Shaw, 1999, Syed, 2013) in engineering practices. According to review of cavity research presented by Rockwell (1978) and Lawson (2011), the cavity geometrical configuration is important in that one must characterize the cavity type but to primarily determine the inherent flow nature. Geometry variation centered on the basic type (rectangular, circular) has been extensively studied (Rockwell, 1978). Conical cavity belongs to circular type which differs from rectangular cavity in that the finite cavity width concept does not exist for conical cavity. Viswanathan (2003) carried out DES numerical simulation of a single conical cavity model in subsonic freestream to resolve large eddy structure inside cavity. Shvets (2003) and Brooker (2017) visualized similar flow pattern and shock/ boundary layer interaction structures in axisymmetric cavities to rectangular cavity. Mohri (2011) performed both laminar and turbulent computation of conical cavity model with various L/D ratio and found that the periodic pressure fluctuations on cavity surface are fundamentally influenced by cavity scale, L/D ratio and boundary layer. Recently, at the request for control enhancement and instability reduction for a new aerodynamic device, Maru *et al*. (2007) proposed a type of modified aerospike instrument (Multiple-Row Disk, MRD) that is implemented by adding stabilizer disks on the aerospike, forming consecutively connected conical cavities. High frequency pressure oscillation through wind tunnel tests in both transonic and supersonic flow regime suggest that a reduction of the pressure oscillation level can be achieved both inside and downstream of the cavities (Maru, 2007). However, additional flow field information beyond the time-resolved pressure measurement is needed to interpret the mechanism responsible for flow oscillation alleviation and the role of the inserted disk in flow stabilization.

The progress of recent computational fluid dynamics (CFD) techniques facilitates economic tools for complex flow field characterizations. To capture the unsteady features of cavity flow, the unsteady Reynolds-Averaged Navier-Stokes (URANS) has been used alongside different turbulence models for equation closure. Even though the time-varying mean flow properties predicated by URANS increased the understanding of the cavity flow, the inherent deficit of this method in predicating the full spectrum of turbulent scales (Lawson, 2011) cannot be eliminated. Large Eddy Simulation (LES) provide the means to solve for larger, energy containing eddies, as well as to accurately capture unsteadiness in the cavity flow field. This method requires enormous computation resource consumption, which makes it difficult to be widely applied, particularly in engineering simulations that have complex geometrical configurations. The Detached Eddy Simulation (DES) was proposed by Spalart (1997) to fix the large turbulent structures in flow field and to achieve a balance between computation costs and resolved turbulent structure. Viswanathan (2003) and Syed (2013) employ the DES simulation to capture both instantaneous and mean flow properties of the cavity field. To avoid grid induced separation in thick boundary layers and shallow separation regions, Delayed-DES (DDES) model was proposed (Spalart, 2006) and based on which Improved Delayed Detached Eddy Simulation (IDDES) model was developed to be allowed to run in Wall-Modeled LES (WMLES) mode in case unsteady inlet conditions (Shur, 2008).

The current investigation utilizes the IDDES method to simulate four selected conical cavity cases in an attempt to extend the understanding of the multiple-row disk configuration. The objectives of the current study comprise of three major components. Initially we validate the credibility and accuracy of the adopted IDDES numerical method by simulating conical cavity flow under high-speed compressible inflow. We then explore the mean flow feature as well as the instantaneous characters that had not yet been addressed through experiments by Maru (2007). Finally, we unveil the underlying flow mechanism that enables the stabilizing of flow oscillation of inserted disks in aerospike. The structure of the paper is organized as follow. Section 2 introduces numerical strategy. Section 3 describes cone cavity model, computational domain and the corresponding grid. Section 4 reports the results obtained through IDDES simulation on four cone cavity cases, in terms of mean and instantaneous flow structure, wall pressure distribution, cavity drag, pressure oscillation characteristics and aeroacoustics. Section 5 summarizes this work.

## 2. COMPUTATIONAL METHODOLOGY

In the current simulation, the finite volume method was employed to solve Navier-Stokes equations. Artificial dissipation was added to solve the invisid

flux with the second-order central scheme. Time discretization uses the implicit Backward Euler method. Turbulence closure utilizes the IDDES method based on the Spalart-Allmaras model. The IDDES method is a hybrid between the RANS/LES method that can automatically divide flow fields into RANS and LES sub regions through scale parameter $\tilde{d}$ . This type of method originates from the detached eddy simulation method, which can smoothly shift from RANS to LES within the boundary layer.

In the S-A based DES model (Allmaras, 2012), eddy viscosity $\nu_t$ is calculated through equations below:

$$\nu_t = \tilde{\nu} f_{v1} \qquad f_{v1} = \frac{\chi^3}{\chi^3 + c_{v1}^3} \qquad \chi = \frac{\tilde{\nu}}{\nu} \tag{1}$$

Where $\nu$ represents kinematic viscosity, $\tilde{\nu}$ is a working variable which can be calculated through Eq.2.

$$\begin{aligned} \frac{D\tilde{\nu}}{Dt} &= c_{b1}(1-f_{t2})\tilde{S}\tilde{\nu} - [c_{w1} f_w - \frac{c_{b1}}{\kappa^2} f_{t2}][\frac{\tilde{\nu}}{\tilde{d}}]^2 \\ &+ f_{t1}(\Delta u)^2 + \frac{1}{\sigma}[\nabla\cdot((\nu+\tilde{\nu})\nabla\tilde{\nu}) + c_{b2}(\nabla\tilde{\nu})^2] \end{aligned} \tag{2}$$

The modified vorticity $\tilde{S}$ in Eq.2 can be calculated with Eq.3.

$$\tilde{S} = S + \frac{\tilde{\nu}}{\kappa^2 \tilde{d}^2} f_{v2} \qquad f_{v2} = 1 - \frac{\chi}{1+\chi f_{v1}} \tag{3}$$

Where $S$ represents vorticity magnitude and $\tilde{d}$ is the distance to the closest wall. Function $f_w$ can be calculated as follows.

$$f_w = g[\frac{1+c_{w3}^6}{g^6 + c_{w3}^6}]^{1/6} \tag{4}$$

$$g = r + c_{w2}(r^6 - r) \tag{5}$$

$$r = \min(\frac{\tilde{\nu}}{\tilde{S}\kappa^2\tilde{d}^2}, r_{\lim}) \tag{6}$$

$$f_{t1} = c_{t1} g_t \exp(-c_{t2}\frac{\omega_t}{\Delta u^2}[\tilde{d}^2 + g_t^2 d_t^2]) \tag{7}$$

$$f_{t2} = c_{t3}\exp(-c_{t4}\chi^2) \tag{8}$$

$$g_t = \min(0.1, \Delta u / \omega_t \Delta x) \tag{9}$$

Where $d_t$ represents distance to the trip point, $\omega_t$ is the vorticity at the trip, $\Delta u$ is the difference in velocity relative the trip point and $\Delta x$ stands for streamwise grid spacing at the trip. Constants included in the model are given in Eq.10.

$$\begin{aligned} &c_{b1} = 0.1355 \quad \sigma = 2/3 \quad c_{b2} = 0.622 \\ &\kappa = 0.41 \quad c_{w1} = c_{b1}/\kappa^2 + (1+c_{b2})/\sigma \\ &c_{w2} = 0.3 \quad c_{w3} = 2 \quad c_{v1} = 7.1 \quad c_{t1} = 1 \\ &c_{t2} = 2 \quad c_{t3} = 1.2 \quad c_{t4} = 0.5 \quad r_{\lim} = 10 \end{aligned} \tag{10}$$

In early DES model, the minimum distance $\tilde{d}$ closest to wall surface is defined as:

$$\tilde{d} = \min(d_w, C_{DES}\Delta) \tag{11}$$

In the equation, $d_w$ represents the distance towards the wall surface, $\Delta$ is mesh scale, $C_{DES}$ is a model constant. The Delayed Detached Eddy Simulation, DDES is based on DES modifies $\tilde{d}$

$$\tilde{d} = d_w - f_d \max(0, d_w - C_{DES}\Delta) \tag{12}$$

The DDES is advantageous in that it avoids triggering the LES mode in advance. The IDDES method combines the DDES method and Wall modeled Large Eddy Simulation （WMLES） method by define $\tilde{d}$ as:

$$\tilde{d} = \tilde{f}_d(1+f_e)d_{RANS} + (1-\tilde{f}_d)d_{LES} \tag{13}$$

$d_{RANS}$ represents RANS scale and $d_{LES}$ stands for LES scale.

$$\tilde{f}_d = \max\{(1-f_{dt}), f_B\} \tag{14}$$

$$f_B = \min\{2\exp(-9\alpha^2), 1.0\} \tag{15}$$

$$\alpha = 0.25 - d_w / h_{\max} \tag{16}$$

$$f_{dt} = 1 - \tanh[(8r_{dt})^3] \tag{17}$$

$$r_{dt} = \frac{1}{\kappa^2 d_w^{\,2}} \times \frac{\upsilon_t}{\max\{[\sum_{i,j}(\partial u_i/\partial x_j)^2]^{1/2}, 10^{-10}\}} \tag{18}$$

$\upsilon_t$ is the eddy viscosity coefficient, $\partial u_i / \partial x_j$ is the velocity gradient, $\kappa = 0.41$.

$$\tilde{d} = d_{WMLES} = f_B(1+f_e)d_{RANS} + (1-f_B)d_{LES} \tag{19}$$

When turbulence fluctuation contained in the free stream, $r_{dt}$ is far less than 1.0, $f_{dt}$ is approximately 1.0, where $\tilde{f}_d = f_B$, and the scale parameter $\tilde{d}$ is convert to

$$\tilde{d} = d_{DDES} = \tilde{f}_d d_{RANS} + (1-\tilde{f}_d)d_{LES} \tag{20}$$

Eq. (21) is applied when choosing the unsteady time step.

$$t < \frac{\Delta_{min}}{V'_{max}} \tag{21}$$

$\Delta_{min}$ is the smallest grid scale and $V'_{max}$ is the maximum fluctuation velocity. In the current study, the unsteady time step is set to a constant of $10^{-5}$, the inner time step is set to 40 guaranteed mass, velocity, and pressure in the outflow boundary converge and maintains a steady value in each time

step.The presented IDDES method had already been successfully used in previous studies (Chen, 2016) where the method was shown to be able to capture and resolve vortex structures in different scales.

## 3. SIMULATION CASE DESCRIPTION

### 3.1 Case Geometrical Configurations

A typical conical cavity geometrical configuration is shown in Fig.1. The basic model that is reproduced from the wind tunnel test model by Maru (2007) is composed of a cone with 8 ° half cone angle and a cylinder that connects with the base of the cone. The axial length of the cone from tip to base is 426.9 mm and the overall length of computational model from cone tip to cylinder base is 500 mm. Four conical cavity cases were implemented based on the basic model. There were five parameters set to control the specific geometrical configuration in each case, as shown in Table 1. According to Fig. 1, S1 represents the longitudinal length from cone tip to the front wall of first cavity. S2 represents the longitudinal length from cone tip to the aft wall of the last cavity. S3 is the thickness of inserted dividing disk. There are slight differences in current cavity length (L) and depth (D) configuration from traditional ones. In the multi-cavity, L and D for each case represent the bottom wall length and front wall depth of the first cavity.

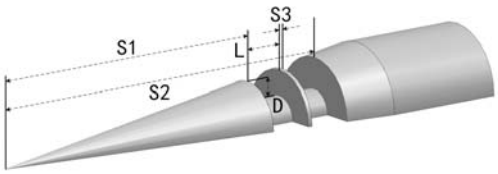


**Fig. 1. The conical cavity geometrical configuration.**

**Table 1 Conical cavity geometrical configuration data, mm**

| case | S1 | S2 | S3 | L | D | L/D |
|---|---|---|---|---|---|---|
| 1 | 360 | 375 | 0 | 15 | 29.14 | 0.51 |
| 2 | 295 | 375 | 0 | 80 | 20 | 4 |
| 3 | 295 | 375 | 4 | 38 | 20 | 1.9 |
| 4 | 295 | 375 | 4 | 24 | 20 | 1.2 |

Case 1 and case 2 are single cavity configurations with the same aft wall location. The different start location on the front wall differentiates the L/D from each other. According to the cavity type classification, case 1 and case 2 are deep and shallow cavity respectively and both of which belongs to open cavity category. In case 3 and case 4, two and three cavities were designed by inserting one and two 4mm thick disks based on the cavity configuration in case 2. The inserted disk equally divides the cavity length in case 2 into two and three smaller ones respectively. Due to the 8° incline of the cone surface, the depth (D) in each cavity in case 3 and case 4 has slight differences between each other. Both case 3 and 4 have a shallow cavity and are the open cavity type.

### 3.2 Computational Domain and Boundary Conditions

The pitch and yaw angle of the model is not considered in the current investigation, so only half of the test model is constructed in grid generation to facilitate the simulation process. The computational domain includes a semi cylindrical farfield boundary with a radius of 10 times of the cone base radius (Fig.2). The cone surface is categorized as a non-slip adiabatic wall boundary. The boundary conditions include the farfield boundary, the none-slip adiabatic wall boundary, the symmetry boundary, and the outflow boundary.

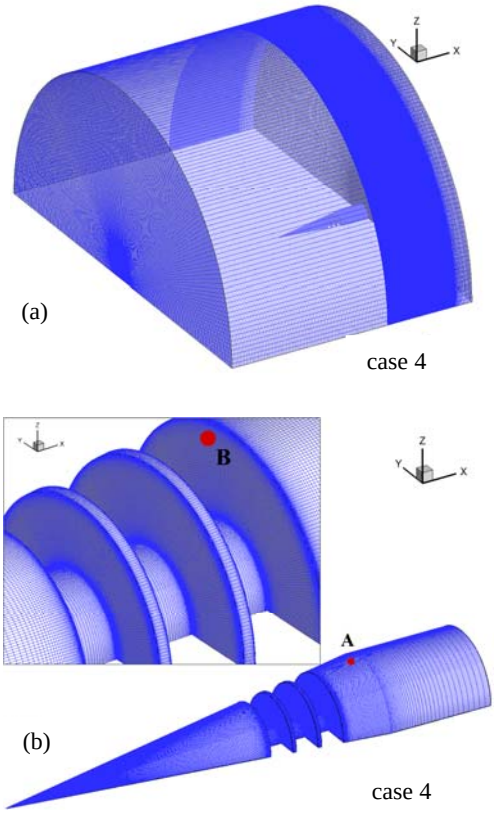


**Fig. 2. Computational domain and grid.**

### 3.3 Grid Generation

To obtain reasonable simulation results in the DES, a grid was generated according to recommendation provide by Spalart (2011). Grid spacing throughout the entire computation domain is constructed differently. In the farfield region, away from cone wall boundary, where the subsonic incoming flow does not induce vorticity. This region is considered the Euler region where isotropic spacing is applied in all three directions to adopt a grid generation consistent with the RANS simulation. The RANS region contains a boundary layer, an initial separation, and a shallow separation bubble that is divided into two sub-regions, the outer region and the viscous region. The viscous region is close to the cone wall surface, the DES method will model viscous sublayer, buffer layer and log layer. The

first spacing $y^+$ was set to 1 and the stretching ratio in the wall normal direction was set to 1.05. The $y^+$ is calculated according to Eq. 22.

$$y^+ = \frac{u_* y}{\upsilon} \tag{22}$$

$u_*$ represents the friction velocity at the nearest wall, $y$ is the distance to the nearest wall and $\upsilon$ is the local kinematic viscosity of the fluid. In the other two directions, the grid-stretching ratio was set to 1.25. In the cavity region that contains a large vorticity value, the wall $y^+$ equal to 1 guarantees that all walls are in a normal direction and grid space stretching ratio is set to 1.1 in all three directions. In LES region that was composed of the wake and evident vorticity generation region, a grid was generated with the same principal as seen in the viscous sub-region in the RANS region. Fig.2 is an example grid of case 4 that shows the farfield boundary grid and the wall boundary grid. The grid generation principal was adopted for all four cases.

### 3.4 Freestream Conditions

Freestream conditions are specified in accordance with wind tunnel experiments data shown in Table.2.

**Table 2 Simulation freestream conditions**

| *Mach* | P*,Pa | T*,K | Re,$10^6$ $m^{-1}$ |
|---|---|---|---|
| 0.9 | 147100 | 288 | 21.9 |

## 4. RESULTS AND DISCUSSIONS

### 4.1 Mean-flow Characteristics

#### 4.1.1 Streamwise Velocity Iso-Surface

Fig. 3 shows the mean iso-surface of streamwise velocity with a value of -15 m/s colored by density. The red and yellow colors represent greater density values. Comparisons made between case 1 and case 2 indicted that the deep conical cavity and shallow conical cavity accommodate different flow structures from inside the cavity. Shear stress is the primary force that expels flow recirculation inside the cavity. In case 1, the reverse flow structure inside the cavity is crushed into scales that match the cavity length. In the transverse direction, reverse structures are divided into individual smaller structures that are unable to bridge the entire cavity. In case 2, by filling the cavity in both the streamwise and transverse directions, a global reverse flow structure was generated. The color painted on the iso-surface in case 1 and case 2 suggests that the flow accumulated in the deep cavity since case 1 is denser than that of shallow cavity （case 2）. The geometry configuration in case 3 and case 4 can be treated as disks that were inserted in case 2, which divides the single cavity into two and three cavities with smaller L/D ratios. The iso-surface indicated that as the cavity L/D ratio decreases, the reverse flow structure tends to maintain the global shape inside the cavity bridge, the front wall, and the aft wall. As the cavity L/D ratio decrease, the density concentrated at the cavity bottom wall corners. Comprehensive comparison made among all four cases indicated that as the conical cavity L/D ratio shrinks, forcing a cavity type transformation from a shallow cavity to a deep cavity, the large reverse structure will be crushed and decomposed into smaller reverse structures inside the cavity.

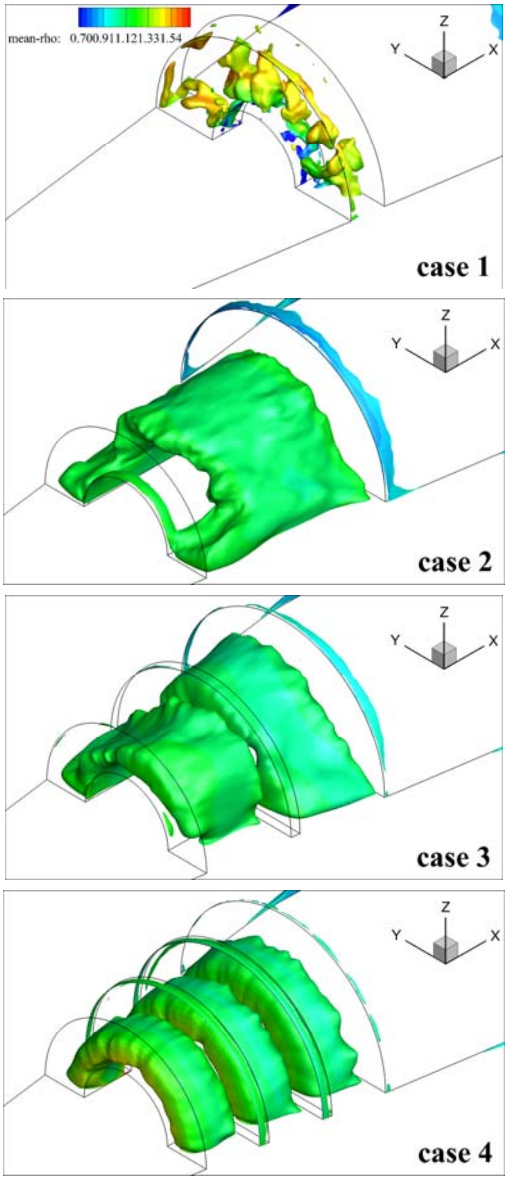


**Fig. 3. Iso-surface of streamwise velocity colored by mean density.**

#### 4.1.2 Wall Pressure Distribution

To explore the influence of different flow structures that are exerted on wall pressure distribution, Fig. 4 plots the mean normalized wall static pressure distribution of all four-cone cavity cases. The dark region in Fig.4 represents the maximum cavity region in flow direction from the first cavity front wall to last cavity aft wall in case 4. This highlights

the cavity region in all cases. The pressure inside the cavity region represents the pressure distribution on the cavity floor. In case 1, there were two pressure peaks on the cavity floor. In case 2, the pressure peak appeared near aft wall. The pressure distribution can be partially interoperated by flow structure shown in Fig.3. In case 1, the smaller and discrete flow structures inside the cavity predominates the pressure distribution on the cavity floor. In case 2, the single global flow recirculation structure generates relatively smooth pressure distribution until the aft wall is reached, which results in the steep pressure increase. Comparisons made between cases 2, 3 and 4 suggest that the division of the single cavity with inserted disks can produce dramatic pressure peaks on the cavity floor. In the cavity downstream cone wall, case 2 had a lower wall pressure than the other cases. In general, the cavity length to depth ratio plays a vital role in determining the flow structure inside cavity, which essentially determines the pressure distribution on the cavity and the cavity downstream wall. The insertion of the disk that divided one single cavity to multiple ones evidently introduced pressure peaks on the cavity floor.

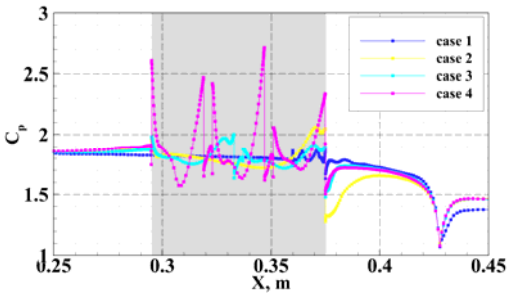


**Fig. 4. Normalized pressure distribution.**

### 4.1.3 Streamwise Velocity Profile

To clarify the cavity influence on the exertion of the downstream flow, Fig. 5 plots the mean streamwise velocity profile in two stands downstream cavities along the cone wall. The corresponding x coordinates were 0.38m and 0.42m. The horizontal coordinates denote the non-dimensional mean streamwise velocity, while the vertical coordinate denotes the vertical distance above the cone wall surface non-dimensioned by reference model length ($L_{ref}$=0.06m). At the X=0.38m stand, there is an evident shear layer in case 2 where the streamwise velocity peak was observed near the cone wall surface. At the X=0.42m stand, the mixing within the outer layer results in a streamwise velocity where case 2, case 3, and case 4 obtain a closely distributed profile. The shear layer accelerated the streamwise velocity in case 1 further than the other cases. This streamwise velocity profile can be further explained using the pressure distribution in Fig.4. The severe entrainment effects in case 2 led to the accelerated flow near the cone aft wall where the decrease in wall static pressure was more evident than in the other cases. Velocity profile downstream of the cavity aft wall alone shows that the division disk inserted in the case 2 cavity weakened the entrainment effects and thus stabilized the boundary layer of the downstream cavity.

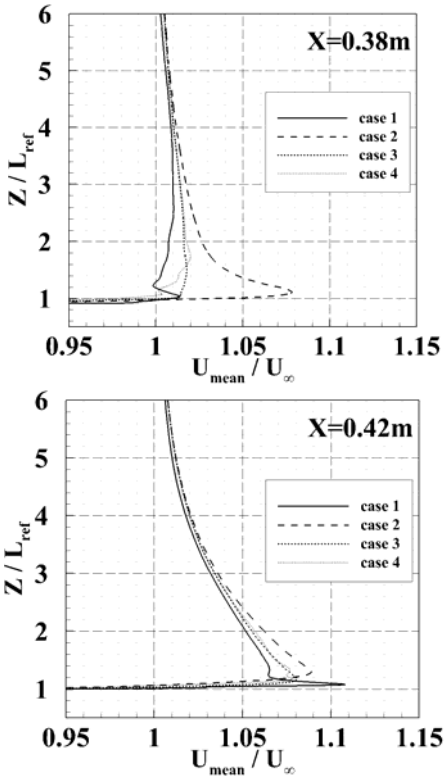


**Fig. 5. Steam wise velocity profile.**

### 4.1.4 Mean-Drag

Cavity drag is an important concern within the study of cavity flow. Table 3 lists the non-dimensionalized drag coefficient by the dynamic pressure head whose reference area is within the cone base area. The drag is an integration of pressure and viscous stress over the entire cone surface, including cone wall and cavity surface. In the single cavity configurations found in case 1 and case 2, a small L/D ratio cavity produced greater drag than the large L/D ratio cavity. The inserted disk in case 2 had a favorable effect in that it reduced the overall cone drag, see Table 3.

**Table 3 Mean-drag**

| | Case 1 | Case 2 | Case 3 | Case 4 |
|---|---|---|---|---|
| $C_d$ | 0.8944 | 0.7174 | 0.7057 | 0.6854 |

## 4.2 Instantaneous Flowfield Analysis

Another important aspect to studying cavity flow is to unveil its instantaneous flow features under specific flow conditions. The following section will provide a detailed flow analysis based on the instantaneous flow data.

### 4.2.1 Energy Spectrum in Wake

To monitor time-resolved wall static pressure, two ports denoted as A and B were implemented

(Fig.2). Port A is located at the cone surface 416.9 mm measure from the cone tip along the axial direction, while port B is located at the last cavity aft wall at a 44.85 mm radius position. Time-resolved static pressure monitored in port A and port B in all four cases are analyzed to obtain power spectral density. As shown in Fig.6, in frequency regimes below $10^3$ Hz, the PSD fluctuates with a stable mean PSD value of approximately $10^2$ $(kPa)^2$/Hz in all four cases in port A. In port B, PSD fluctuates more violently than that in port A in this frequency regimes. In high frequency regimes above $10^3$ Hz of both port A and B, energy content gradually decreased as frequency increased in cases 2, 3 and 4. In case 1, the PSD plot showed an evident difference from the other cases. Case 1 initially increased to the maximum value and then subsequently decreased. The primary focus was the energy decay in the cavity eddy and wake region, and the PSD plot differences between case 1 and the other three cases will be discussed in subsequent section. It was observed that for all four cases, when the frequency regime was above 104 Hz, the energy content decreased in the larger to smaller structures with an approximate slope value of -5/3, which is in accordance with Kolmogorov's energy spectrum. This demonstrated the capability of the current IDDES scheme to simulate the correct flow physics with energy cascade in both inside and downstream cavity region.

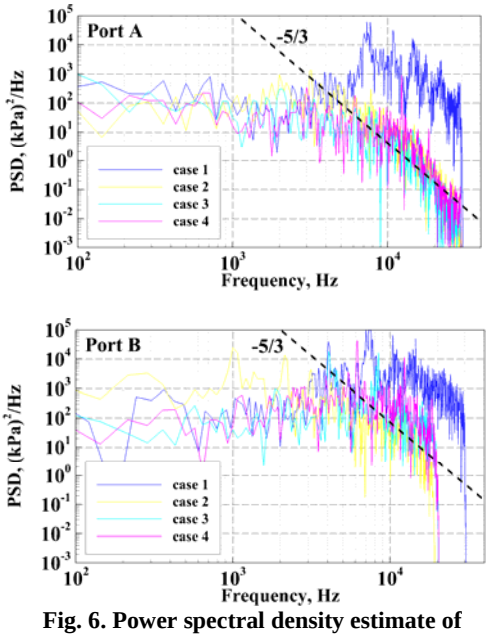


**Fig. 6. Power spectral density estimate of pressure data in wake.**

### 4.2.2 Instantaneous Flow Structure

The instantaneous iso-surfaces of Q-criteria for all four cases are shown in Fig. 7 to visualize the flow structures. The iso-surface at Q=108 is colored with a Mach number ranging between 0.1 and 1.3. The iso-surface highlights the swirl structure around the cavity region. The swirl begins a bit upstream of the cavity leading edge. In all four cases, hairpin vortices formed downstream of the leading edge of the front cavity wall, however, the onset position are slightly different for each case. In case 1, a large-scale hairpin vortices leg were initially found at the mid-section of the cavity, and the vortices head stretch into main flow. Case 2 differed from the rest in that the hairpin vortices size and scale was comparatively larger. In case 3 and case 4, the hairpin vortices formed near the rear wall of the last cavity. In the cavity downstream region, large vortices decayed dramatically.

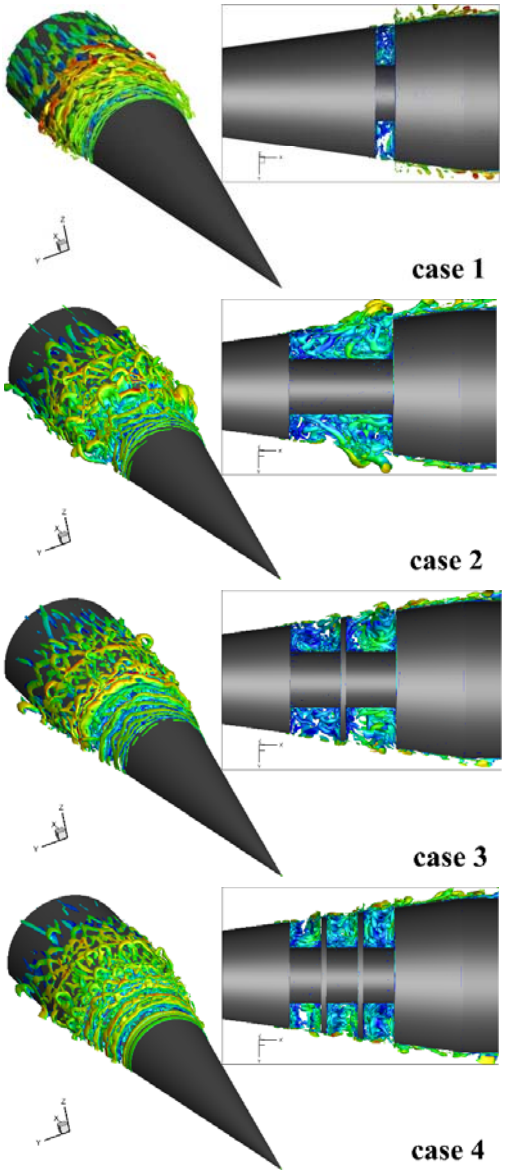


**Fig. 7. Instantaneous iso-surface of Q-criteria colored by Mach number.**

The instantaneous vorticity contour for all four cases is shown in Fig. 8. There is one slice on the symmetry plane and another slice perpendicular to the symmetry plane that creates a three-dimensional view inside the cavity. The color legend in each figure is set to capture the most evident vortical structure. The orange and red colors in the contour represent vorticity exceed 26211 $s^{-1}$. In case 1 and case 2, it was observed that the shear layer that

separated from the leading edge of cavity initially maintained its flow direction with the cone surface and then broke down. In case 3 and case 4, the shear layers were similar to case 1, as it was solely found in the first cavity of the multiple cavities. Comparison made between case 2 and case 3 suggested that the inserted disk in case 3 changed the flow pattern inside the cavity and the cavity downstream region dramatically. In case 2, the shear layer breakdown was approximately 30% of cavity length, which was in accordance with observations made in the rectangular cavity (Ashcroft, 2005). In case 3, the shear layer breakdown took place for about 50% of the cavity length. In case 2, the large vorticity gathered around both the rear wall of cavity and the downstream outside of the cavity. In case 3, flow structure inside was influenced by the first cavity. At the rear wall region of the second cavity, the vorticity concentration and the downstream outside of the cavity was expelled.

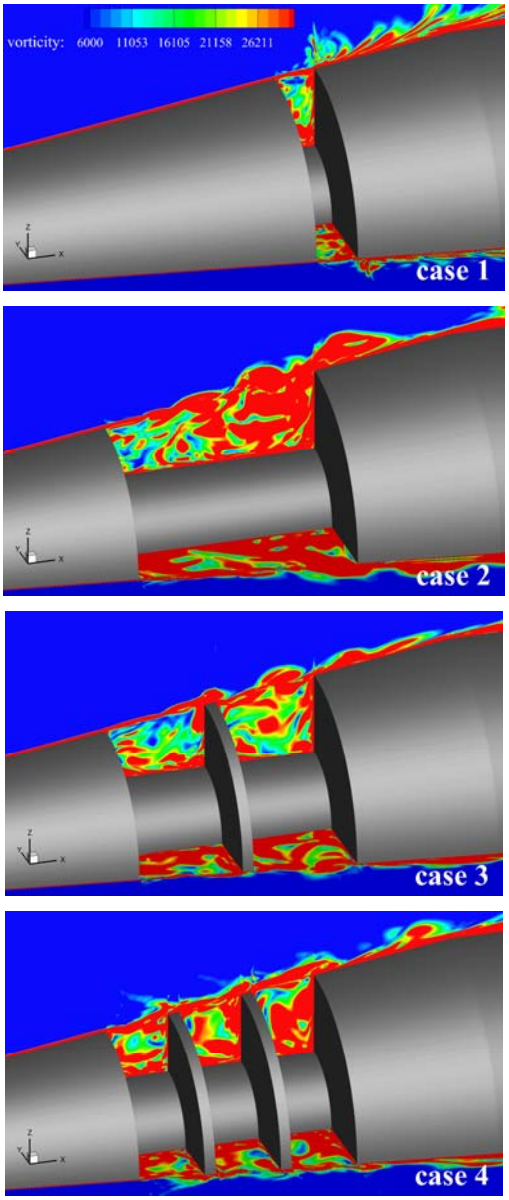


**Fig. 8. Instantaneous vorticity contour.**

### 4.2.3 Pressure Oscillation Characteristics

Pressure oscillation frequency is an important parameter in evaluating unsteady cavity flow characters. The time-resolved wall static pressure at port B was recorded for power spectral density analysis. Fig.9 showed power spectral density in four cases. In general, the PSD peaks exist within a frequency range of 1~14 KHz with PSD peak value below 50 K $(kPa)^2/Hz$. As previously defined in section 3.1, case 1 is deep cavity and case 2, 3, 4 are shallow cavities. Rockwell (1978) suggested that the self-sustaining oscillations in both deep and shallow cavities can be characterized as fluid-resonant oscillations which usually exhibit high oscillation frequency, but the dominant instability mechanisms are different for shallow and deep cavities. Flow oscillations in case 1 is characterized by the motion of strong transverse waves which can be partially interpreted with the flow structure inside cavity. In Fig.8 case 1, the shear layer bridge almost the entire cavity from front corner to aft corner through which shear layer instability effects is reduced. The streamwise velocity iso-surface in Fig.3 case 1 suggests that the non-existence of longitudinal flow structure fosters the propagation of transverse waves within cavity. In comparison, in case 2, 3 and 4, the PSD fundamental frequency increases with the shrink of longitudinal flow structure within cavity (Fig.3, case 2, 3 and 4). Flow oscillations in case 2, 3 and 4 is characterized by the coupling effects of longitudinal wave motion and shear layer instability (Fig.8, case 2, 3 and 4).

Rossiter (1964) developed a semi-empirical equation to predict pressure oscillation in rectangular cavity based on the cavity experiments conducted at subsonic and transonic freestream conditions. To include higher sound speed effects, Heller (1970) modified Rossiter's equation as shown is Eq.23.

$$f_n = \frac{U_\infty}{L} \times \frac{n-\alpha}{[M_\infty / \sqrt{1+(r/2)(\gamma-1)M_\infty^2}] + (1/k_c)} \quad (23)$$

Where $k_c = 0.57, \alpha = 0.25, r = 0.1$

Table 3 lists the cavity pressure oscillation frequencies predicated by modified Rossiter semi-empirical equation, experimental data (Maru, 2007), and current numerical simulations. In case 1 and case 2, the cavity length L used in Eq. 18 is the cavity flow length in case 3 and case 4, where L is the last cavity floor length. CFD results were obtained through power spectral analysis through a time-resolved static pressure data in monitor A. In case 1, the pressure oscillation frequencies analyzed through CFD data and experimental data in three modes were higher than the theoretical predications. The experimental predicated first mode frequencies were about two times over obtained results and the CFD data was about 28% higher. In case 2, both the experimental data and the CFD results predicted a close value, as suggested by the semi-empirical calculation. In the multi-cavities configurations seen in case 3 and case 4, the CFD predicted about 1.7 times the fundamental frequency than the theoretical calculation. Two major factors can

influence the frequency discrepancy. First, Rossiter (1964) developed the correlation based on large experiments carried out on rectangular cavities. The special L/D ratio in case 1 might have gone beyond the applicable range of Eq. 18. Second, in case 3 and case 4, the pressure data used for the PSD analysis is monitored in the last cavity. The incoming flow, particularly the boundary layer at the corner of the last cavity, is different from the clean cavity. The incoming flow condition can exert influence on the cavity oscillation frequency.

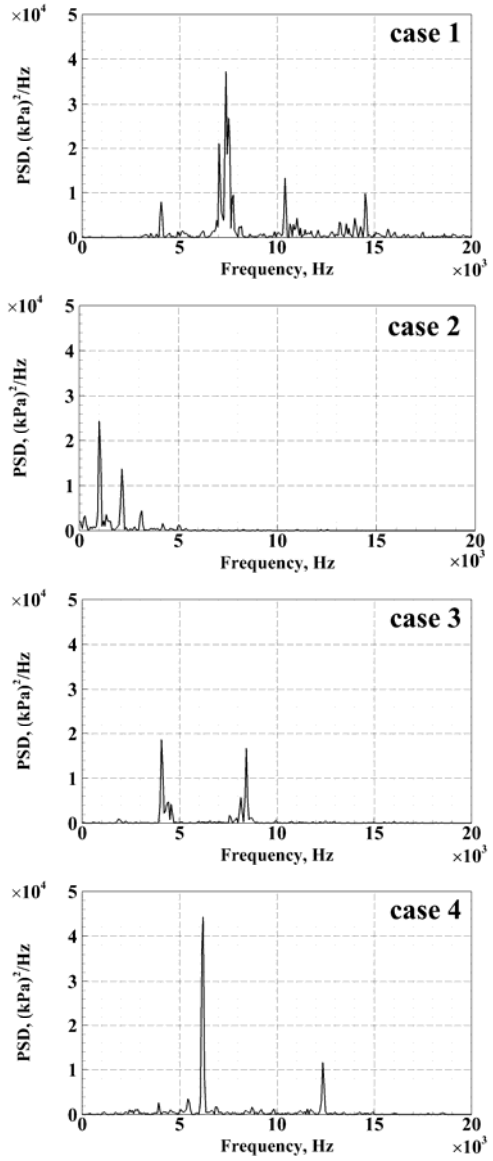


**Fig. 9. Power spectral density estimated with pressure data inside cavity.**

### 4.2.4 Correlativity Analysis

To analyze the cross-correlation of pressure signals on different monitor stations, the cross power spectral density of the pressure signal was calculated using Eq.24, where $R_{xy}(m)$ is computed according to Eq.25. $P_{xy}(\omega)$ estimated the cross power spectral density of the discrete-time signals x and y using the Welch's averaged, modified periodogram method of spectral estimation, where xn and yn are jointly stationary random processes, and E {·} is the expected value operator.

$$P_{xy}(\omega) = \sum_{m=-\infty}^{\infty} R_{xy}(m) e^{-j\omega m} \tag{24}$$

$$R_{xy}(m) = E\{x_{n+m} y^*_n\} = E\{x_n y^*_{n-m}\} \tag{25}$$

**Table 4 Cavity pressure oscillation frequencies**

| case | Mode | Theoretical, Hz | Exp [Maru,2007], Hz | CFD, Hz |
|---|---|---|---|---|
| 1 | 1st Mode | 5760 | 12366 | 7381 |
| | 2ed Mode | 13439 | 25114 | 10424 |
| | 3rd Mode | 21119 | 37557 | 14555 |
| 2 | 1st Mode | 1079 | 992 | 998 |
| | 2ed Mode | 2520 | 2097 | 2161 |
| | 3rd Mode | 3960 | / | 3831 |
| 3 | 1st Mode | 2274 | / | 4071 |
| | 2ed Mode | 5305 | / | 8411 |
| | 3rd Mode | 8336 | / | / |
| 4 | 1st Mode | 3600 | / | 6214 |
| | 2ed Mode | 8400 | / | 12375 |
| | 3rd Mode | 13199 | / | / |

Figure 10 depicts the cross power spectral density of pressure signal of case 2 and 3 both inside and downstream of the cavity. Dots in each graph mark pressure monitor ports. The pressure signals are generally in weak correlation with each other as the cross power spectral density $P_{xy}(\omega)$ in each case lays within $\pm 1.0$. In case 2, the corelativity of 1 and 2 is stronger than that of 1 and 3. In contrast, in case 3, the corelativity of 1 and 4 is stronger than that of 3 and 4. The phenomena suggest that without the inserted division disk, the pressure oscillation correlation between the upstream cavity and the inside cavity is stronger. The self-sustained feedback mechanism established this strong connection between the upstream cavity and the inside cavity. With the insertion of division disk, this feedback mechanism was cut and a new mechanism wa established to cover the last cavity and downstream flow.

### 4.2.5 Acoustic Predictions

The sound pressure level was calculated based on the power spectral density data that is obtained through the Fourier transformation with the surface static pressure on the cavity aft wall denoted as point B. Sound Pressure Level (SPL) and Overall Sound Pressure Level (OASPL) are obtained through Eq.26 and Eq.27.

$$SPL = 20log_{10}\left(\frac{\sqrt{PSD(P)}}{P_{ref}}\right) \tag{26}$$

$$OASPL = 20log_{10}\left(\frac{P_{rms}}{P_{ref}}\right) \tag{27}$$

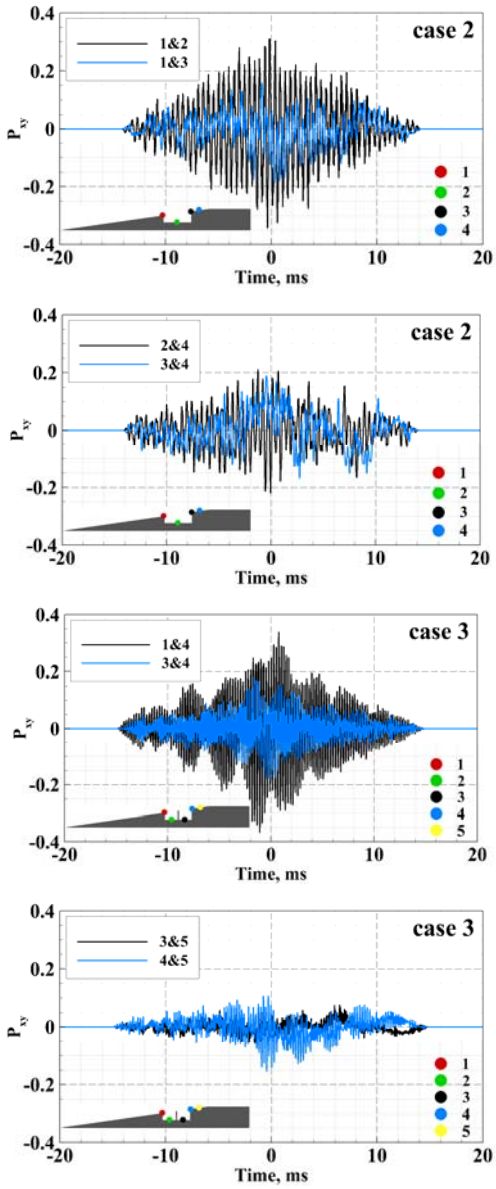


**Fig. 10.Correlativity coefficient.**

Figure11 shows the SPL plots according to numerical results. As shown, in frequency regime [0, 10000Hz] and tonal modes in cases 1, 3 and 4 showed a similar pattern. They all had two apparent peaks in this regime. According to experimental data Maru (2007), the SPL level in case 1 has three tonal modes that correspond to frequencies of 10000, 25000 and 38000 Hz. The simulation is marginally resolved in the first mode; however, the second and third mode was not properly captured. In case 2, the SPL tonal modes frequencies are apparently lower than in case 1. This is due to the PSD property shown in both experiments and simulations. According to experiments by Maru (2007), the peak value of SPL exceeds 160 dB, which corresponds to the 1000 Hz frequency. The frequency was captured by simulation, where the peak SPL value was under estimated. Comparisons made among the SPL data in cases 1, 3 and 4 showed that the SPL is dominated by the cavity geometrical configuration (L/D ratio). Even though the cavity exists before the last cavity in case 3 and case 4, the SPL characteristics at the aft wall of the last cavity present analogous behavior.

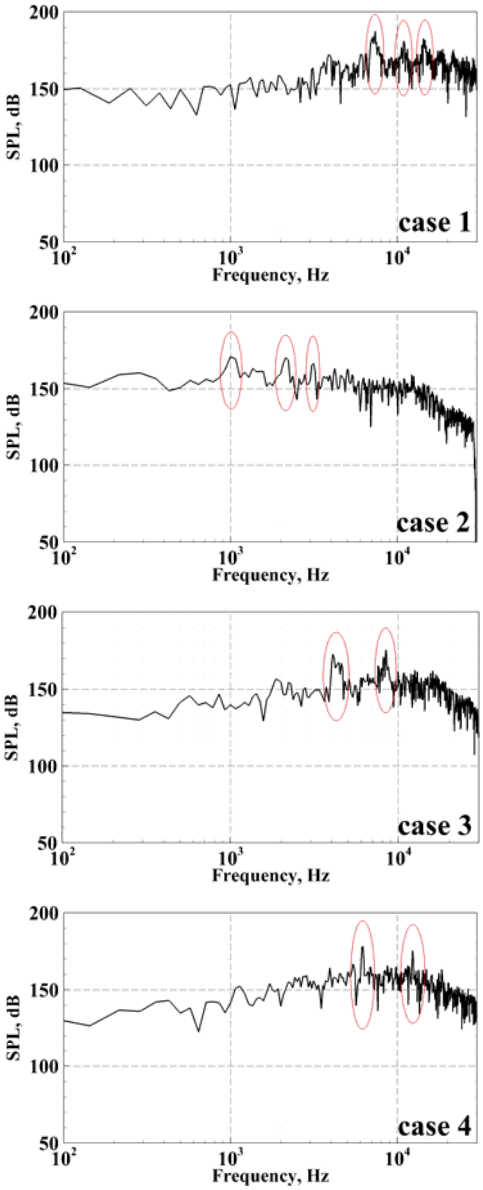


**Fig. 11. Sound pressure level.**

The overall sound pressure level is plotted in Fig.12 to evaluate the acoustic level inside the cavity. The horizontal coordinate represent the axial distance along the cone centerline while the vertical coordinate is the overall sound pressure level. The data point in Fig.12 is calculated with the pressure recorded on the cavity floor. As shown in Fig.11, the OASPL in case 1 is about 45 dB lower than the other cases. The inserted disk in case 2 that divided the shallow cavity into two and three smaller ones could not inherently change the primary flow feature inside the cavity and consequently cannot change the OASPL level inside the cavity.

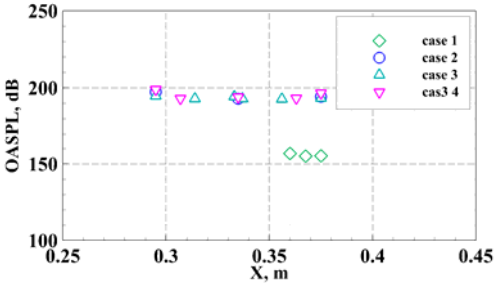


**Fig. 12. Overall Sound pressure level.**

## 5. CONCLUSIONS

Aerodynamic characteristics of four configurations of cone models with different length to depth ratios and various cavity numbers were numerically evaluated in the current study. Pressure oscillation and acoustic resonance are primarily dominated by the geometrical configuration (L/D) in each single cavity. In case 1 where L/D equals 0.51, the pressure oscillation in acoustic resonance mode resulted in high frequency pressure oscillation. Both the numerical predicated oscillation frequency and the experimental data given by Maru （2007） in the three modes were higher than the modified Rossiter empirical predication. In case 2, the cavity length was increased to where L/D equals 2, and the pressure oscillation in the self-sustained oscillation mode where the oscillation frequency was captured by both numerical results and the experimental prediction.

Through the insertion of the disk in case 2, the cavity configuration in case 3 and case 4 were formed. The entrainment observed in case 2 can be alleviated and the overall cone drag can be reduced. The primary flow structure in case 3 and case 4 was likely inherited from case 2 without dominant changes. The insertion of disk can effectively modulate the pressure oscillation peak frequency as well as the acoustic tone. The overall sound pressure level inside cavity will not be changed until the geometrical adjustment seen in case 1.

## ACKNOWLEDGEMENTS

This work was supported by National Natural Science Foundation of China through Grant No. 51276151, No. 91441128 and No. 11602209. Authors wish to gratefully acknowledge high performance computation resource support from Hypersonic Research Lab of Xiamen University.

## REFERENCES

Allmaras, S. R.; F. T. Johnson and P. R. Spalart (2012). Modifications and Clarifications for the Implementation of the Spalart-Allmaras Turbulence Model, *Seventh International Conference on Computational Fluid Dynamics (ICCFD7), Big Island, Hawaii*, ICCFD7-1902.

Ashcroft, G., and X. Zhang (2005). Vortical structures over rectangular cavities at low speed. *Physics of Fluids* 17(1), 152.

Brooker, B. T., N. S. Chaganti, R. Weiner and S. M. Olcmen (2017). Flow Characteristics of Axisymmetric Cavity. *55th AIAA Aerospace Sciences Meeting, Grapevine, Texas*. AIAA 2017-1475.

Chen R., X. Wang and Y. You (2016) Numerical simulation of nacelle's effects on propeller slipstream based on IDDES model. *Acta Aeronautica et Astronautica Sinica*, 37(6), 1851-1860.

Heller, H. H., D. G. Holmes and E. E. Covert, (1970). Flow-induced pressure oscillations in shallow cavities. *Journal of Sound and Vibration* 18(4), 545-546.

Heller, H., and D. Bliss (1975). The physical mechanism of flow-induced pressure fluctuations in cavities and concepts for their suppression. *2nd Aeroacoustics Conference, Hampton, VA, U.S.A.* AIAA 75-491.

Lamp, A. M. and N. Chokani (1997). Computation of cavity flows with suppression using jet blowing. *Journal of Aircraft* 34(4), 545-551.

Lawson, S. J. and G. N. Barakos (2011). Review of numerical simulations for high-speed, turbulent cavity flows. *Progress in Aerospace Sciences* 47(3), 186-216.

Maru, Y., H. Kobayashi, S. Takeuchi and T. Sato (2015). Flow oscillation characteristics in conical cavity with multiple disks. J*ournal of Spacecraft and Rockets* 44(5), 1012-1020.

Maull, D. J. and L. F. East (1963). Three-dimensional flow in cavities. *Journal of Fluid Mechanics* 16(4), 620-632.

Mohri, K. and R. Hillier (2011). Computational and experimental study of supersonic flow over axisymmetric cavities. *Shock Waves* 21(3), 175-191.

Rockwell, D. and E. Naudascher (1978). Review—Self-Sustaining Oscillations of Flow Past Cavities. *Journal of Fluids Engineering.* 100(2), 152-165.

Rockwell, D. (1977). Prediction of oscillation frequencies for unstable flow past cavities. *Journal of Fluids Engineering* 99(2), 294-300.

Rossiter, J. E. (1962). The effects of cavities on the buffeting of aircraft. *RAE Technical Memorandum* Aero 754.

Rossiter, J. E. (1964). Wind-tunnel experiments on the flow over rectangular cavities at subsonic and transonic speeds. *RAE Technical Report* 64037.

Sarno, R. L. and M. E. Franke (1994). Suppression of flow-induced pressure oscillations in cavities. *Journal of Aircraft*, 31(1), 90-96.

Sarohia, V. and P. F. Massier (1977). Control of cavity noise. *Journal of Aircraft*, 14(9), 1275-1279.

Sarohia, V. (1977). Experimental investigation of

oscillations in flows over shallow cavities. *AIAA Journal* 15(7), 984-991.

Shaw, L. and S. Northcraft (1999). Closed loop active control for cavity acoustics. *AIAA* 1999-1902.

Shur, M. L., P. R. Spalart, M. K. Strelets and A. K. Travin (2008). A hybrid rans-les approach with delayed-des and wall-modelled les capabilities. *International Journal of Heat and Fluid Flow*, 29(6), 1638-1649.

Shvets, A., M. Gilinsky and I. Blankson (2003). Wind tunnel results for gas flows inside axisymmetric cavities on cylindrical bodies with nose cones. *12th AIAA International Space Planes and Hypersonic Systems and Technologies.* AIAA 2003-7064.

Spalart, P. R. (2011). Young-Person's Guide to Detached-Eddy Simulation Grids. *NASA TM Report* CR-2001-211032.

Spalart, P. R., S. Deck, M. L. Shur, K. D. Squires, M. K. Strelets and A. Travin (2006). A new version of detached-eddy simulation, resistant to ambiguous grid densities. *Theoretical and Computational Fluid Dynamics* 20(3), 181.

Stallings Jr, R. and F. Wilcox Jr (1987). Experimental cavity pressure distributions at supersonic speeds. *Technical Paper* 2683, NASA.

Syed, S. A. and K. A. Hoffmann (2013). Detached eddy investigation of cavity resonance phenomenon in slender cavities. *Journal of Aircraft* 50(3), 982-985.

Unalmis, O. H., N. T. Clemens and D. S. Dolling (2001). Experimental study of shear-layer/acoustics coupling in Mach 5 cavity flow. *AIAA Journal*, 39(2), 242-252.

Viswanathan, A. K., K. D. Squires and J. R. Forsythe (2003). Detached eddy simulation of the flow over an axisymmetric cavity. *AIAA Aerospace Sciences Meeting and Exhibit*. AIAA 2003-0265.